

DATA-EFFICIENT ONE-STEP MECHANICAL DESIGN OF COMPOSITES USING GENERATIVE AI

MILAD MASROURI^{1,2}, ZHAO QIN^{1,2,3*}

1 Department of Civil and Environmental Engineering, Syracuse University, Syracuse, NY 13244, USA, mimasrou@syr.edu

2 Laboratory for Multiscale Material Modeling, Syracuse University, 151L Link Hall, Syracuse University, Syracuse, NY 13244, USA, zqin02@syr.edu

3 The BioInspired Institute, Syracuse University, NY 13244, USA

*Materials & Correspondence should be addressed to Dr. Zhao Qin (zqin02@syr.edu)

Key words Generative Artificial Intelligence, Stable Diffusion, composite design, Low-Rank Adaptation, Molecular Dynamics Simulation.

Abstract. The distribution of material phases is crucial to determine the composite's mechanical properties. While the entire structure-mechanics relationship of highly ordered material distributions can be studied with a finite number of cases, this relationship is challenging to reveal for complex irregular distributions, preventing the design of such material structures from meeting specific mechanical requirements. The noticeable developments of artificial intelligence algorithms in material design enable the discovery of hidden structure-mechanics correlations, which is essential for designing composites of complex structures. It is intriguing how these tools can assist composite design. Here, we focus on the rapid generation of complex irregular composite structures and the stress distribution in loading. We find that generative AI, enabled through fine-tuned Low-Rank Adaptation models, can be trained with a few inputs to generate synthetic composite structures and the corresponding von Mises stress distribution. The results show that this technique is convenient in generating massive composite designs with useful mechanical information that dictates stiffness, fracture, and robustness of the material with one model, and such must be done by several different experimental or simulation tests. This research offers valuable insights for improving composite design to expand the design space and automatic screening of composite designs for improved mechanical functions.

1 INTRODUCTION

Composites are multi-phase materials composed of two or more distinct materials, typically in the form of a matrix and a reinforcement with different mechanical properties. Composites excel beyond traditional materials in various engineering fields such as aerospace [1], defense [2], automotive [3], healthcare [4], and construction [5]. The optimization of composite designs

has become crucial in modern engineering, enabling the combination of multiple advanced mechanical functions that individual components cannot achieve on their own, such as stiffness [6], toughness [7], elasticity [8], ultimate strength [9], and thermal conductivity [10]. Traditional manufacturing methods have limited the design and production of complex geometric arrangements in composite materials due to challenges in effectively bonding multiple base materials with strong adhesion [11]. However, advancements in additive manufacturing have made it possible to 3D print various materials, allowing the design and production of complex architectures with diverse properties in all three spatial dimensions and with any geometry and combination of distinct materials [12]. Nature offers numerous examples of composite materials that demonstrate the benefits of integrating multiple material phases, refined over millions of years of evolution [13][14]. Almost all natural materials exhibit composite structures, typically composed of a limited set of polymeric substances such as proteins or polysaccharides, along with ceramic components like calcium salts or silica, which are themselves composites [15][16][17]. For instance, bone is a natural composite consisting of a collagen matrix reinforced with hydroxyapatite, providing both strength and flexibility [18]. Other examples include nacre [19], a biomineral composite of calcium carbonate crystals embedded in an organic matrix, and bamboo [20], a natural composite of cellulose fibers embedded in a lignin matrix. Principles derived from exceptional biological composites include: (i) the integration of rigid and soft materials for combined strength and toughness [21][22][23], (ii) the formation of robust three-dimensional interconnections between phases to distribute loads and dissipate energy effectively [24][25], and (iii) the alignment of structurally anisotropic elements to enhance performance in specific orientations [25]. Interpenetrating phase composites (IPCs) are a type of composite material where two or more phases are interconnected in a continuous and intertwined manner, creating a complex microstructure [26]. This unique configuration differentiates IPCs from traditional composites, where one phase is typically dispersed within another in a more straightforward manner (e.g., fibers within a matrix). The design of IPCs has advanced significantly, leveraging bioinspired architectures to achieve superior mechanical properties. Studies have demonstrated that IPCs with bioinspired architectures, such as brick-and-mortar, Bouligand, and crossed-lamellar, exhibit enhanced stress transfer, damage delocalization, and crack arresting mechanisms, leading to improved strength, toughness, and impact resistance compared to traditional composites [27]. Research on 3D-printed Mg-Ti IPCs, for instance, has highlighted the effectiveness of these designs in providing a synergistic enhancement in both strength and fracture toughness, making them suitable for structural and biomedical applications [28]. The continuous and interpenetrated phases in these composites mimic the intricate arrangements found in natural materials, contributing to their exceptional mechanical efficiency [29].

Optimizing composite mechanics *per se* has become a fundamental question: how to decide the material distribution that yields the optimal material functions? Having an efficient tool to facilitate design and reveal the structure-mechanics relationship will help give a quick answer to the question and lead to material innovations for broader engineering applications. MD simulations, particularly when executed with precise force fields, yield highly accurate predictions of the mechanical response of nanomaterials, including the atomistic scale molecular behavior level and large-scale stress field [30][31][32]. However, they are computationally demanding and can easily exceed the available computational capacity if used to produce massive data for brute-force designing and optimization purposes. In contrast, deep

learning has arisen as a promising solution for tackling this challenge, offering an alternative to first-principle methods like MD or finite element methods (FEM) [33]. It acts as an auxiliary model for MD and FEM by integrating the constitutive relationship and differential equations and simply replacing the correlation functions, which accelerates mechanical behavior prediction [34]. It also enables the massive consideration and comparison of different design configurations and the use of the results to make material design and rational reverse design possible [35]. However, most of these supervised learning methods are limited by the high training data and the quality requirements. They prevent it from being used in research applications because pioneering research usually lacks data, and the available data must be better structured.

Since 2022, artificial intelligence generated content (AIGC) has performed exceptionally well and garnered significant interest from researchers. AI-based image generators, including DALL-E 2 [36], Imagen [37], Midjourney [38], and Stable Diffusion (SD) [39], have emerged as a notable area of study. The main objective of these generative AI algorithms is to create new synthetic images that accurately replicate the patterns found in their training dataset [40]. Among these tools, SD is a generative AI model enabled through image diffusion in the latent space, which facilitates the synthesis of high-resolution images by leveraging perceptual and semantic compressions. This model has proven effective across various applications, including text-to-image [41], text-to-video [42], and super-resolution [43]. Compared to traditional diffusion models [44], SD offers greater computational efficiency, enabling the creation of higher-resolution images. Unlike the original generative adversarial networks (GANs) [45], SD does not suffer from mode collapse or training instabilities. The success of these models suggests the possibility of applying generative AI to process a small amount of data/image and use the augmented data/image for rational design and optimization. While these models have demonstrated their ability to produce realistic images [39][46][47], their potential for material design and characterization remains largely unexplored. Similar to Large Language Models (LLMs) like GPT by open AI [48], developing special-purpose SD models that are experts in specific tasks or scientific domains can be costly, especially when diverse sets of capabilities are required. However, methods like Low-Rank Adaptation (LoRA) [49], Differential Learning Rates (DLR) [50], Prompt Tuning [51], and Full Model Fine-Tuning [52] have been proposed as a more efficient way to fine-tune a pre-trained model by updating the weights and make the model improve its ability for specific tasks. For example, Buehler has utilized LoRA to fine-tune an LLM, creating MechGPT, which leverages LLMs to improve multiscale modeling of materials failure. [53]. Another fine-tuned LLM, BioinspiredLLM, highlights the potential for AI to accelerate research and scientific discovery in bio-inspired materials [54]. In another study, X-LoRA was presented as a mixture-of-experts, framework enhancing LLMs with LoRAs for specialized tasks in protein mechanics and molecular design [55]. Zhao et al. employed LoRA to train a special-purpose SD model that can efficiently generate remote sensing image-annotation pairs, drastically reducing the time and effort required for detailed pixel-level annotations in semantic segmentation [56]. In our recent research [57], we explored the ability of a fine-tuned SD model to simultaneously generate a bicontinuous composite structure and its corresponding von Mises stress field. We demonstrate that the model is highly data-efficient and successfully captures the essential mechanical characteristics of a bicontinuous composite under load. These studies demonstrate LoRA's effectiveness in fine-tuning general-purpose models into specialized experts focusing on a target scientific domain.

LoRA is a training strategy designed to accelerate the training of large models while reducing memory usage, commonly employed for specific, targeted tuning. In LoRA modeling, the principle involves integrating low-rank matrices with the original full-scale matrix, where these low-rank matrices are the sole trainable components of the model. This approach allows the model to retain the extensive knowledge acquired during its initial pre-training phase while adapting more specifically to particular tasks [49].

Here, to efficiently generate composite designs with complex material distributions and quickly reveal their mechanical responses under loading, we develop a workflow that integrates physics-based models with Generative AI (GenAI). As shown in Fig. 1, this workflow involves steps such as dataset generation, GenAI model training, and model validation. We use a phase-field model to create IPCs with complex material distributions and employ molecular dynamics (MD) simulations to determine the mechanical responses of these composites under loading. The resulting stress fields are then used to fine-tune a pretrained Stable Diffusion model using LoRA to tailor it for stress field prediction in IPCs. This approach allows for the rapid generation of complex composite structures and their corresponding stress distributions when subjected to external loads. We demonstrate that the generated results differ from the training inputs and that the stress fields can be validated through MD simulations. Our models can massively generate composite designs with stress distributions, enabling the prediction of vulnerable areas and leading to improved material design with enhanced mechanical properties.

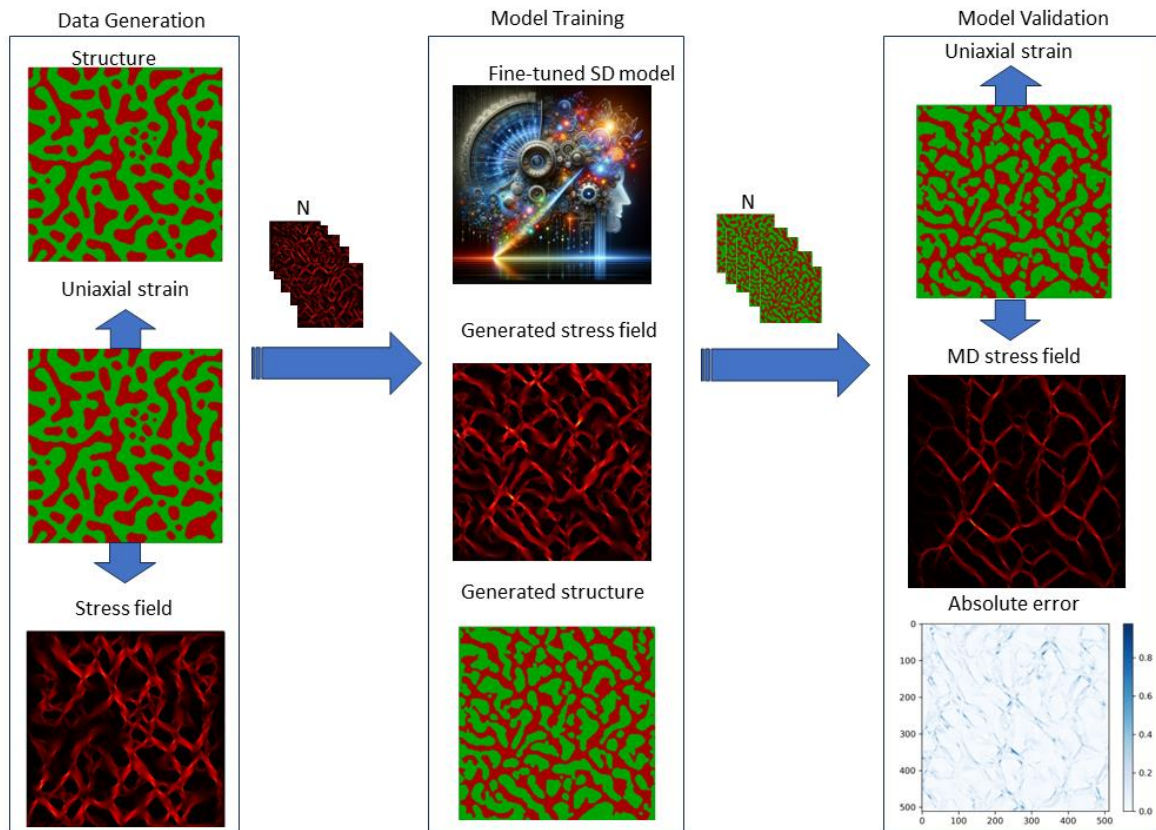


Figure 1: Workflow of the Study: Data Set Generation, Model Training, and Model Validation.

2 MATERIALS AND METHODS

2.1 Phase field model to create the initial composite structures

We use phase field model to simulate the evolution of microstructure in a binary composite during phase transformations and pattern formation. It represents the material microstructure with continuous field variables that describe the spatial distribution of phases or components. The evolution of these field variables is governed by partial differential equations derived from thermodynamic principles and kinetic laws. The primary equation in the phase field model is the Cahn-Hilliard equation which is represented as:

$$\frac{\partial u}{\partial t} = \nabla^2 \left[\frac{df(u)}{du} - \theta^2 \nabla^2 u \right] \quad (1)$$

where $-1 < u(x,y,t) < 1$ is the difference in concentration of the two phases, with $u < 0$ denoting the soft and $u \geq 0$ representing the rigid phases, t is the evolutionary time of the system, $f(u)$ is the free energy function, and θ is the width of transition region between the two phases. In our study, we adopt the double-well potential function $f(u) = \frac{1}{4}(u^2 - 1)^2$ and set $\theta = 0.004$. A two-dimensional IPC structure is generated by solving Eq. (1) in a square box which is discretized into $N \times N$ lattice, where N is sufficiently large taken to be $N = 256$. We define u_{ijk}^m denoting the discrete value of $u(ib, jb, m\tau)$ at lattice node point (ib, jb) , where b and τ are the mesh size and the integration time step, respectively. Discretizing Eq. (1) with central approximation of spatial derivatives results in the following discrete equation:

$$\frac{u_{ij}^{m+1} - u_{ij}^m}{\tau} = \nabla^2 [(u_{ij}^m)^3 - u_{ij}^m - \theta^2 \nabla^2 u_{ij}^m] \quad (2)$$

where $\nabla^2 u_{ij}^m = [u_{(i+1)j}^m + u_{(i-1)j}^m + u_{i(j+1)}^m + u_{i(j-1)}^m - 4u_{ij}^m]/b^2$ is used to approximate the continuous Laplacian on the discrete lattices. To numerically solve Eq. (2), an adaptive integration time step τ should be properly selected. Numerical tests suggest that $\tau = 0.00001$ is an appropriate choice that ensures high accuracy, good stability, and reasonable computational cost. A set of initial values $u(ib, jb, 0)$ are randomly generated, and periodic boundary conditions are adopted in x and y directions of the box. A cutoff u_c^m is set to distinguish the soft phase from the rigid phase. The phase of point $u(ib, jb)$ at time $t = m\tau$ is defined as:

$$G_{ij}^m = H(u_{ij}^m - u_c^m) \quad (3)$$

where $H(u_{ij}^m - u_c^m)$ is the standard step function. When $u_{ij}^m > u_c^m$, $H(u_{ij}^m - u_c^m) = 1$, indicating that the point is occupied by rigid phase; otherwise, $H(u_{ij}^m - u_c^m) = 0$, showing that the point belongs to the soft phase. Table 1 summarizes the parameters used in our model along with their values.

Table 1: Parameters adopted to generate the structures following phase field model.

Parameter	Value
N	256
θ	0.004
b	1/128
τ	0.00001

t_{total}	200000
-------------	--------

The process of data set generation begins with the creation of 150 random models through the phase field model. In Fig. 2b, an example of these structures is shown, with green indicating the presence of rigid component and red denoting the soft phase. In this study, we build the structures with a volume fraction of 55% wt of rigid and 45% wt of soft, resulting in the emergence of some soft inclusions (depicted in red) dispersed within the rigid matrix (depicted in green).

2.2 Elastic Network Model to model mechanics of the composite materials

We use a triangular elastic network of mass and springs to model the mechanics of each material phase in composite structures. This model enables us to compare the deformation and stress field of the composites by performing MD simulation. Each particle in the composite structure is considered a bead which is bonded to neighboring particles by a spring (Fig.2a). In a triangular lattice, each bead is connected to six neighboring beads, forming a hexagonal pattern. The area associated with each bead can be determined by calculating the area of the hexagon and considering that each bead effectively occupies one-third of this area. The total area of a hexagon, which consists of six equilateral triangles with side length a , is $\frac{3\sqrt{3}}{2}a^2$. Since each bead contributes to one-third of this hexagonal area, the area per bead in the lattice is $\frac{\sqrt{3}}{2}a^2$. In a triangular elastic network with N beads and $3N$ bonds, the deformation energy can be calculated by:

$$U = \frac{3}{2}k\delta^2N \quad (4)$$

where δ is the elongation of a bond, N is the total number of atoms and k is stiffness of a bond. The deformation energy of a triangular lattice can also be derived by considering the energy per unit volume due to uniform deformation. The bulk modulus K relates to the energy density and the strain with $u = \frac{1}{2}K\varepsilon^2$. The total deformation energy U is given by multiplying the energy density by the total volume, which includes the area per bead, the thickness t , and the number of beads N . Substituting the relationship $K = \frac{E}{3(1-2\nu)}$ into the energy equation, where E is Young's modulus and $\nu=0.05$ is Poisson's ratio, we obtain:

$$U = \frac{\sqrt{3}}{2.7}E\delta^2tN \quad (5)$$

Using Eqs. (4) and (5), we have:

$$k = \frac{\sqrt{3}}{4}Et \quad (6)$$

which is the stiffness of each bond at zero deformation. To incorporate the bond rupture, each bond is modelled by a Morse potential in which the bond energy and bond force is therefore given by:

$$U = D[1 - e^{-\alpha(r-a)}]^2 \quad (7)$$

$$f = \frac{dU}{dr} = 2D\alpha e^{-\alpha(r-a)}[1 - e^{-\alpha(r-a)}] \quad (8)$$

here, D and α are parameters related to the potential energy, and a represents the initial length of the spring, corresponding to the lattice constant of the triangular network. The bond stiffness is obtained by:

$$k = \frac{d^2U}{dr^2}(r = a) = 2D\alpha^2 = \frac{\sqrt{3}}{4}Et \quad (9)$$

Considering Eqs. (8) and (6), the bond strength is given by:

$$\max(f) = \frac{1}{2}D\alpha = \frac{\sqrt{3}}{3}Et * \delta = \frac{\sqrt{3}}{3}Et \frac{\sigma_c}{E} a = \frac{\sqrt{3}}{3}\sigma_c t a \quad (10)$$

Combining Eqs. (9) and (10), we can obtain Morse potential parameters by $\alpha = \frac{3E}{16\sigma_c a}$ and $D = \frac{32\sqrt{3}}{9}\sigma_c^2 a^2 t/E$.

We summarize the numerical value of the potential parameters of the two material phases in Table 2. We use mechanical properties of Agilus 30 black as the soft and digital ABS plus as the rigid material.

Table 2: The numerical values of the potential parameters used in the computational simulations in LAMMPS. Micro units are used to perform simulations and obtain parameters in table.

Parameter	Rigid phase	Soft phase
Material thickness t (μm)	1	1
Young's modulus E ($\text{pg} \cdot \mu\text{m}^{-1} \cdot \text{ms}^{-2}$)	973000	383
Ultimate strength σ_c ($\text{pg} \cdot \mu\text{m}^{-1} \cdot \text{ms}^{-2}$)	30000	700
Bond stiffness k ($\text{pg} \cdot \mu\text{m}^{-2}$)	4.21×10^5	165.84
Bond length a (μm)	0.373	0.373
Bond parameter α ($1. \mu\text{m}^{-1}$)	16.304	0.275
Bond energy D ($\text{pg} \cdot \mu\text{m}^{-2} \cdot \text{ms}^{-2}$)	792.529	1096.183

2.3 MD Simulation setup and parameters

We simulate uniaxial strain in 2D composite structures in LAMMPS package [58] with Morse potential and micro units. The sample geometry is varied by randomly changing the distribution of soft and hard materials following phase field model to generate the training data. Each sample is meticulously relaxed to its minimum energy configuration using the conjugate gradient method prior to the application of any external loads. After that, using a Nosé-Hoover thermostat, the samples are thermally equilibrated at 300 K for 40 μs . We use 2 ns as the time step and apply periodic boundary conditions in x - y dimensions. The simulation box is stretched with a constant strain rate ($0.0001 \mu\text{s}^{-1}$) in the y -direction to create uniaxial tension as it is shown in Fig. 2. To create the dataset, we subject the structures to an external load for a duration of only 10 μs . This brief exposure allows us to observe the initial stress distribution under relatively low external loads and to remain in the elastic region. OVITO [59] is used to visualize the atomic structures, dynamics, and stress fields. Images portraying the von Mises stress fields at a strain of $\varepsilon = 0.008$, within elastic region, are processed and collected as the ground truth

for the training dataset. The ‘‘hot’’ color map is used for visualizing these stress field contours, which spans from ‘‘black’’ [RGB = (0, 0, 0)], indicating a lower limit stress of 0.02 MPa, to ‘‘white’’ [RGB = (255, 255, 255)], representing an upper limit stress of 15 MPa. Although the specific lower and upper bounds may differ across various cases, they remain uniform within our dataset. Ultimately, the images were saved with a resolution of 2048×2048 pixels.

2.4 Stable diffusion image generator

We employ generative AI enabled through SD models for image generation and fine-tune a pre-trained SD model using the Low Rank Adaptation (LoRA) method, tailoring it specifically for generating IPC composite stress field images under tensile load.

SD is based on the foundational diffusion approach, specifically denoising diffusion probabilistic models. This method involves two main phases: the forward phase and the backward phase (Fig. 3a). In the forward phase, noise is incrementally added to an original image in a controlled manner, with each step of added noise adhering to a specific normal distribution. This process transforms the original image into one that is completely obscured by noise. During the backward phase, denoising modules that resemble the architecture of a U-Net are trained to predict and remove the noise that was added during the forward phase. This denoising process is carried out step by step, starting from the fully noised image and gradually restoring it to resemble the original image. Once the denoising modules are effectively trained, the model can reconstruct images from their noised states, reversing the noise addition process. The general term formula for the forward process can be expressed mathematically:

$$x_t = \sqrt{\alpha_t}x_{t-1} + \sqrt{1 - \alpha_t}\epsilon_t \quad (11)$$

where x_t is the image at timestep t , x_{t-1} is the image at the previous timestep, ϵ_t represents the noise added at step t , which is sampled from a normal distribution, and α_t is a parameter to describe the noise intensity with $0 \leq \alpha_t < 1$. As t increases, more noise is added to x_t , making it less recognizable as the original image x_0 . The entire forward processing can be rewritten as:

$$x_t = \sqrt{\bar{\alpha}_t}x_0 + \sqrt{1 - \bar{\alpha}_t}\epsilon_t, \epsilon_t \in \mathcal{N}(0, I), \bar{\alpha}_t = \prod_{i=1}^t \alpha_i \quad (12)$$

The coefficients $\{\alpha_t\}$ are predetermined and its value decreases for each step t , guiding how the original image is gradually converted into a noise-dominated image by the end of the forward process (i.e., $x_t \rightarrow \epsilon_t$). This noised image then serves as the starting point for the backward process, where the model learns to denoise the image step by step, ultimately recovering an approximation of x_0 . In the backward processing phase, under the assumptions of a Gaussian process and Markov chain, the objective is to progressively denoise the image, moving from a state of high noise back to the original or a close approximation of the original image. The mathematical formulation for this process is focused on iteratively estimating and removing the noise added during the forward phase to recover the clean image. The general term formula for the backward process, at a timestep t , can be expressed as:

$$x_{t-1} = \frac{1}{\sqrt{\bar{\alpha}_t}} \left(x_t - \frac{1 - \alpha_t}{\sqrt{1 - \bar{\alpha}_t}} \epsilon_\theta(x_t, t) \right) + \eta_t z_t, z_t \in \mathcal{N}(0, I) \quad (13)$$

where the first term represents the t step recovered image, $\epsilon_\theta(x_t, t)$ is the model’s estimate of the noise added at time t , that is, the output of the denoising U-Net, $\eta_t = \frac{1 - \bar{\alpha}_{t-1}}{1 - \bar{\alpha}_t}$ is a parameter controlling the amount of stochasticity or randomness reintroduced at step t , and z_t is a random

noise vector sampled from a Gaussian distribution.

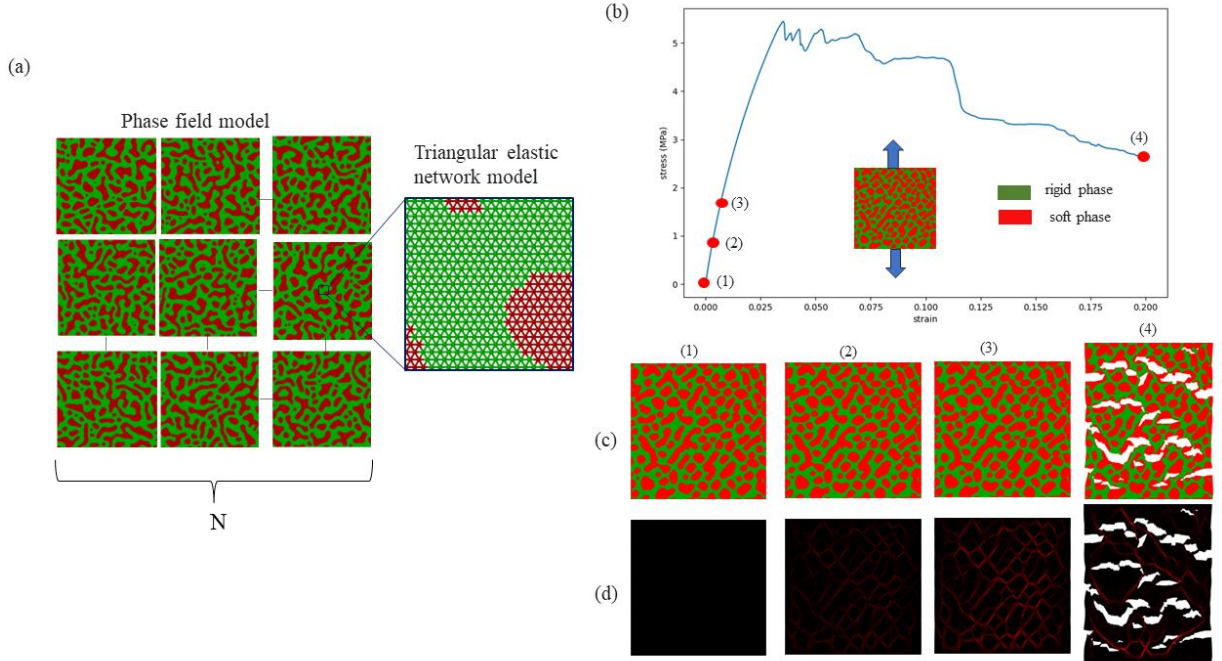


Figure 2: a) Random IPC structures generated by the phase-field model alongside a schematic of the triangular elastic network model. In the image, the red color represents the soft phase, while the green color indicates the rigid phase. The ratio of the phases is controlled during phase field model to create structures with $V_{\text{rigid}} = 55\%$ wt, $V_{\text{soft}} = 45\%$ wt volume ratio (a) Stress-Strain curve from coarse-grained MD simulation. (b) Internal structure of the composites with different strain states (i.e., (1) $\varepsilon = 0$ (2) $\varepsilon = 0.002$ (3) $\varepsilon = 0.008$ (4) $\varepsilon = 0.2$) that correspond to the marks in panel (b), and (d) Von Mises stress distribution related to the corresponding strain levels shown by red dots on the curve.

In the workflow, the process starts with a stress field image x_0^L . In forward processing, the noise is systematically introduced to x_0^L following Eq. 11 for t times. The culmination of this phase is x_t^L . The backward processing phase begins with x_t^L . The image undergoes a denoising process aimed at restoring it to the original image, x_0^L , by Eq. 13. Once the U-Net is adequately trained to predict and negate the noise, it becomes capable of generating any number of stress field images from a given set of arbitrarily noised images. Fig. 3a illustrates the pixel space transformations for clarity. However, most forward and backward processing happens in the latent space.

As illustrated in Fig. 3b, SD begins by compressing the original image from its pixel format (x) into a more compact latent representation (z) using the encoder ε of a Variational Autoencoder (VAE). The model then undergoes forward processing, resulting in z_T . The model is then refined through backward processing with a denoising U-Net, which aims to remove noise and reconstruct z from z_T . Lastly, the VAE decoder \mathcal{D} translates this refined latent representation (z) back into the original pixel space (\tilde{x}), completing the image generation process. The transformer τ_θ encodes the input prompt into a highly informative form for the subsequent image generation steps, ensuring that the final output is a visual representation that

matches the prompt's description. Regarding the network details, the diffusion step number t of x_t^L in Fig. 3a was set to 40, implying that the denoising process in the diffusion model is conducted through 40 distinct U-nets in each iteration.

2.5 Technical details of LoRA method

To limit the generation of stress field images in the training dataset's pixel distribution and to accelerate the training process, we integrate the LoRA method into a pre-trained model. We apply LoRA to a pre-trained SD model to guide it toward generating the stress field of IPCs under load. The LoRA block number was the same as the pre-trained model (Fig. 3c). Unlike complete parameter tuning methods that necessitate updating all weights during the fine-tuning phase, LoRA retains the weights of the original model and integrates trainable low-rank matrices to the transformer layers to simulate the weight adjustment. Fig. 3d presents the mechanism of LoRA. Suppose $W_0 \in R^{d \times k}$ as the matrix from the pre-trained model. LoRA approximates the transition from W_0 to $W_0 + \Delta W$ in the following manner:

$$W_0 + \Delta W = W_0 + W_{down}W_{up} \quad (14)$$

where $W_{down} \in R^{d \times r}$ and $W_{up} \in R^{r \times k}$, with $r \ll \min(d, k)$. W_0 is held constant throughout the fine-tuning stage, but W_{down} and W_{up} are the adjustable parameters. For any given input x with its original output h , the updated output \bar{h} is calculated as:

$$\bar{h} = W_0x + \Delta Wx = h + W_{down}W_{up}x \quad (15)$$

When fine-tuning the SD model, LoRA can be explicitly employed on the cross-attention layers (Figs.3b-c) that are responsible for establishing connections between image representations and corresponding descriptive prompts.

2.6 Model training

We train eight LoRA-tuned SD models using varying numbers of stress field images from our collection pool of 150 IPC composite structures. Specifically, the models were trained with 2, 5, 10, 25, 50, 100, 125, and 150 images, designated as T2, T5, ..., and T150, respectively. To ensure a robust evaluation and mitigate the influence of selection bias, we employed a randomized selection process to draw images from our training set. This methodological approach was designed to rigorously evaluate the impact of training set size on model performance while minimizing potential subjectivity in the selection process. The selected training images were adjusted to a resolution of 2048×2048 . Our training utilizes the stable-diffusion-v1-5 pre-trained model, adopting a batch size of 1, a training duration of 10 epochs, and a learning rate of 0.0001 without any adjustments (constant learning rate schedule). Optimization was performed using the AdamW8bit optimizer, facilitating effective network adjustment. The training hyperparameters are detailed in Table 3. The training procedure is conducted using the open-source Kohya SS library in Python.

Table 3: Summary of the hyperparameters used to fine-tune SD model using LoRA technique.

Parameter	Value/Type
-----------	------------

Lora Type	Standard
Model checkpoint file	stable-diffusion-v1-5
Learning rate	0.0001
Batch size	4
Learning rate scheduler	Constant
LR warmup (% of steps)	10
Optimizer	AdamW8bit
Network Rank (dimension)	128
Network Alpha	1
Number of epochs	10
Mixed precision	fp16
Save precision	fp16
Number of CPU threads per core	2
Maximum resolution	512,512
Minimum bucket resolution	128
Maximum bucket resolution	2048
Text Encoder learning rate	0.00005
Unet learning rate	0.0001

2.7 Stress field generation

We employ a text-to-image approach to generate stress field images from the trained models. A predefined text prompt is the input for the text-to-image approach, guiding the model to generate random stress field images. Subsequently, a binary mask is applied to these images to transform the stress fields into their initial configurations so that the MD simulation is performed, and the obtained stress field is compared with the generated stress field. Image generation uses the open-source "Automatic 1111" GUI [60], a user-friendly platform for interaction with the SD model.

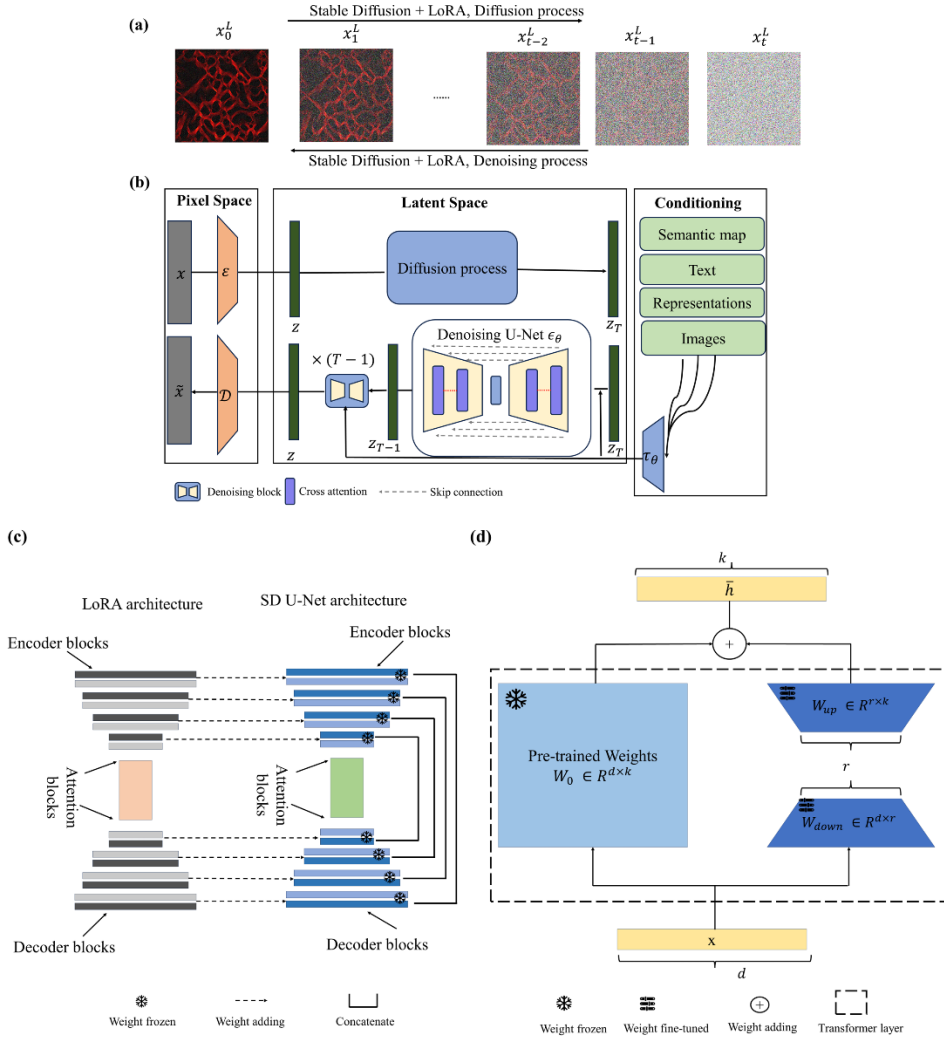


Figure 3: Overall procedure and network architecture of LoRA-tuned SD model (a) An illustration showing how diffusion and denoising processes are carried out by integrating LoRA and pretrained SD models. The model ultimately learns to create an image from complete noise based on the input text prompt. Although these tasks occur in latent space, they are presented in pixel space for clarity. (b) SD architecture (c) details of SD denoising module and LoRA (d) The core components of LoRA and mechanism of fine-tuning a pre-trained SD model, showing how the weights of the pre-trained model are fine-tuned by LoRA matrices according to Eqs. 14 and 15.

2.8 Image normalization and comparison

Using OpenCV, PIL, and NumPy Python libraries, we first convert generated RGB images into grayscale using:

$$\sigma_{gray} = 0.2989R_{\sigma_{RGB}} + 0.5870G_{\sigma_{RGB}} + 0.1140B_{\sigma_{RGB}} \quad (16)$$

where σ_{gray} is the matrix of pixel values for a grayscale image, and $R_{\sigma_{RGB}}$, $G_{\sigma_{RGB}}$, and $B_{\sigma_{RGB}}$ are the red, green, and blue components of the σ_{RGB} matrix. Next, we normalize σ_{gray} , adjusting pixel values to fall between 0 and 1 using:

$$\bar{\sigma} = \frac{\sigma_{gray} - \min(\sigma_{gray})}{\max(\sigma_{gray}) - \min(\sigma_{gray})} \quad (17)$$

Then $\bar{\sigma}$ is turned into a 2D configuration through the application of a binary mask combined with a threshold using:

$$\Omega = \begin{cases} 1 & \text{if } \bar{\sigma} < \theta \\ 0 & \text{otherwise} \end{cases} \quad (18)$$

where Ω is the matrix of binary configuration, and θ is a defined threshold. These configurations are then subjected to uniaxial strain in LAMMPS (refer to Materials and Methods section 2.3), and the resulting stress fields are compared to the ground truth images.

To facilitate the comparison and evaluation of the models, we postprocess both synthetic and ground truth images. After cropping and resizing to 512×512 , we use Eqs. 16 and 17 to obtain $\bar{\sigma}_{synthetic}$ and $\bar{\sigma}_{ground}$ as the normalized pixel value of the generative image and MD output. This step ensures uniformity and enhances contrast. For accuracy assessment, we calculate the Root Mean Squared Error (RMSE) between the ground truth and synthetic images

by $\overline{RMSE}_{stress} = \sqrt{\frac{1}{N} \sum_{i=1}^N (\bar{\sigma}_{synthetic_i} - \bar{\sigma}_{ground_i})^2}$, where N is the total number of pixels in the images, $\bar{\sigma}_{synthetic_i}$ and $\bar{\sigma}_{ground_i}$ are the pixel values at the i -th position in $\bar{\sigma}_{synthetic}$ and $\bar{\sigma}_{ground}$, respectively. Additionally, the absolute error map is calculated for each pixel to visually highlight discrepancies between the synthetic and the ground truth values. This map effectively summarizes the model's performance by illustrating where and how $\bar{\sigma}_{synthetic}$ and $\bar{\sigma}_{ground}$ differ. The absolute error is computed by $\overline{Error}_{stress} = |\bar{\sigma}_{synthetic} - \bar{\sigma}_{ground}|$. We also calculate Structural Similarity Index (SSIM) between each pair of synthetic and ground truth images.

3 RESULTS AND DISCUSSION

We have developed eight SD models as described in the Materials and Methods section 2.6. Each model is trained using a unique text prompt, such as "a photo of an IPC stress field," to direct the generation of images. Post-training, we evaluate the models' performance through both quantitative metrics and qualitative assessments.

3.1 Mode collapse analysis

Mode collapse is a phenomenon observed in generative models, such as Generative Adversarial Networks (GANs), where the model produces a limited variety of outputs despite the diverse training data. This issue occurs when the generator, instead of learning to produce a wide range of outputs, generates only a few types of outputs that the discriminator cannot easily distinguish from real data. Consequently, the generator repeatedly produces similar outputs, resulting in a lack of diversity and exploration in the generated data. To evaluate the occurrence of mode collapse in our data generation process, we compute the Structural Similarity Index (SSIM) matrix for the generated images and training images for models T5, T50, and T100, as summarized in Fig. 4. The results indicate that the SSIM between generated and training images is low, suggesting that the new structures exhibit significant diversity and

uniqueness, effectively mitigating the risk of mode collapse. This common issue in generative models limits output variety and restricts exploration of the design space. However, the consistently low SSIM values between any pair of generated images, as shown in Fig. 4, demonstrate the robustness of our model against mode collapse. This indicates the model's capability to explore a broad and varied design landscape, facilitating the generation of diverse and distinct structures, which is essential for effective generative modeling.

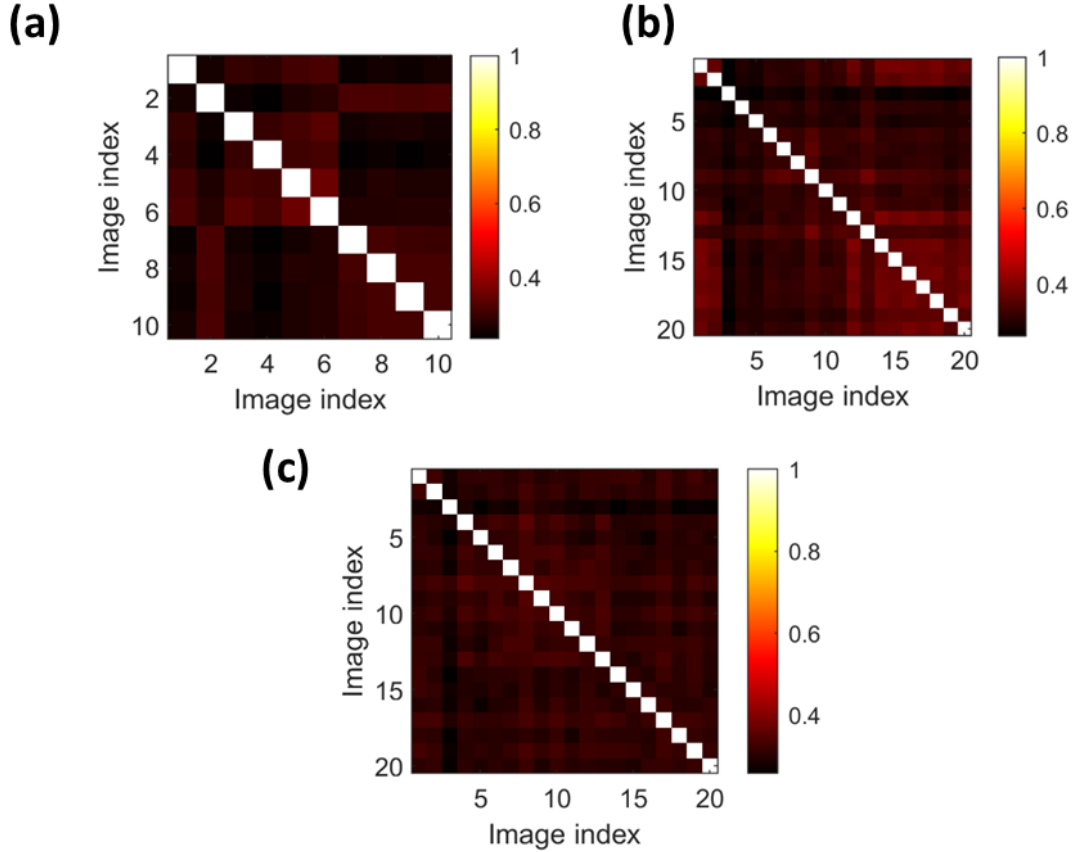


Figure 4: SSIM analysis of generated images and training images for (a) T5 (index $\in [1,5]$ for generated, index $\in [6,10]$ for training), (b) T50 (index $\in [1,10]$ for generated, index $\in [11,20]$ for training), and (c) T100 Models (index $\in [1,10]$ for generated, index $\in [11,20]$ for training).

3.2 Analysis for stress prediction errors and distributions

3.2.1 Qualitative analysis

Fig. 5 compares two synthetic images alongside their actual ground truth counterparts. Our analysis reveals that the models successfully capture key features, including stress concentration on rigid phase, especially on thinner regions, meaning that those regions are prone to crack initiation and failure of the structure. The synthetic stress fields display a von Mises stress value close to zero in the soft phase, indicating that the rigid phase bears the majority of the load. This observation aligns well with the ground truth stress fields.

3.1.2 Quantitative analysis

For evaluating the accuracy of the models, we use pixel-wise root mean square deviation (RMSE) and the structural similarity index (SSIM). Pixel-wise RMSE quantifies the dissimilarity between two images by calculating the square root of the average squared differences in pixel values. This involves determining the squared differences in intensity values for corresponding pixels, reflecting the disparity in stress levels at specific locations. The resulting single numerical value encapsulates the overall difference in pixel intensities, offering a measure of how effectively one image aligns with another in terms of stress intensity. Since there is no specific RMSE threshold that defines good model performance, we use SSIM to enhance our understanding of the models' performance, recognizing that a diverse set of metrics provides a more comprehensive assessment. SSIM evaluates the perceived quality of two images by analyzing their structural information, including luminance, contrast, and structure. Unlike pixel-wise RMSE, SSIM considers these aspects in its assessment. The SSIM index is computed by analyzing the mean, standard deviation, and cross-covariance of these components, ultimately providing an overall index that ranges from -1 to 1, where higher values indicate greater structural similarity between the images. Fig. 5 shows the comparison between the synthetic images (generated by Generative AI) and the ground truth images (LAMMPS output) for two structures. The pixel-wise difference map highlights variations in stress distribution by contrasting the values of corresponding pixels. The normalized RMSE values demonstrate that the model achieves a sufficient level of accuracy, making it suitable for predicting stress distribution within random IPC composite structures. However, it is important to note that the SSIM values, which quantify structural similarity, do not reach the ideal level of 100% similarity (1). We assume that an SSIM higher than 0.5, when accompanied by a sufficiently small RMSE, indicates satisfactory alignment of stress distribution.

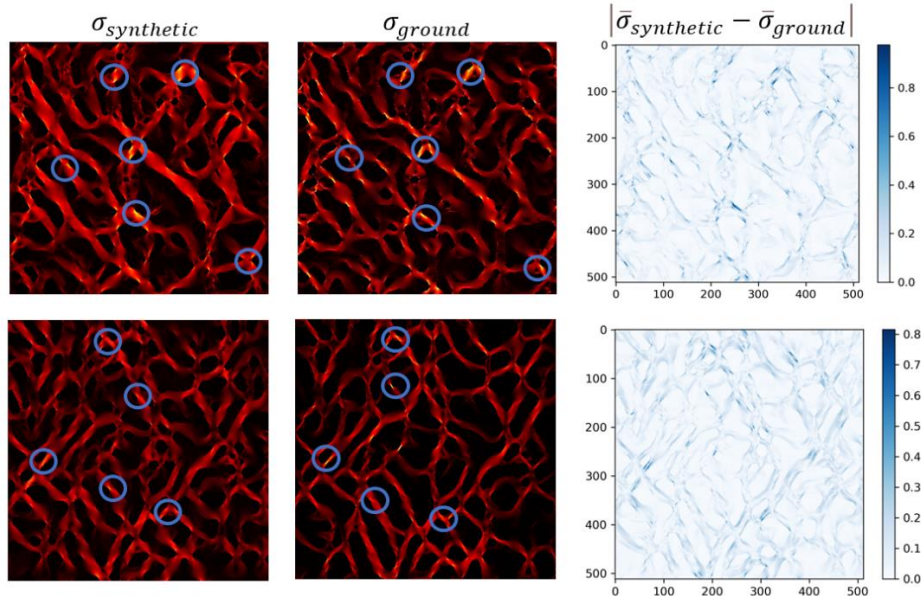


Figure 5: Comparison between synthetic and the corresponding ground truth stress fields. The error map employs a "Blues" heatmap to represent normalized error values, where lighter pixels correspond to lower errors and darker blue pixels indicate higher error magnitudes.

3.1.2.1 Effect of training data size on model's performance

To assess the impact of the number of training images on the precision of the LoRA model, we train models T2, T5, T10, T25, T50, T100, T125, and T150. For each model, we generate 10 images and repeat the model validation process by comparing synthetic images with their corresponding ground truth images. The comparison shown in Fig. 6 demonstrates that while there is no significant visual improvement in the accuracy of the models with an increasing number of training images, the ability of the model to explore and generate a diverse range of structures improves with more training data. Models trained with fewer images (e.g., T2) tend to be biased towards the limited training data, leading to a smaller design space. In contrast, models trained with more images (e.g., T100, T150) are capable of designing more varied and unique structures, indicating a broader and richer design space.

In Fig. 7a, we present the RMSE and SSIM values for each model. Notably, the lowest RMSE value is observed T100, whereas the T125 model demonstrates the highest SSIM value. To select the most accurate model, we undertake a process of normalizing the RMSE and SSIM values and then calculate the aggregate error. Higher RMSE values denote heightened error levels, whereas lower SSIM values signify increased error. The combined error considers the normalized RMSE and SSIM values, standardizing them onto a uniform scale, for the computation of the overall error associated with each model. The combined error is calculated by Eq. (19).

$$\text{Combined error} = \omega_1 * RMSE_{\text{norm}} + \omega_2 * SSIM_{\text{norm}} \quad (19)$$

where $RMSE_{\text{norm}} = \left(\frac{RMSE - \min(RMSE)}{\max(RMSE) - \min(RMSE)} \right)$, $SSIM_{\text{norm}} = \left(\frac{\max(SSIM) - SSIM}{\max(SSIM) - \min(SSIM)} \right)$, $\omega_1 = 0.5$ and $\omega_2 = 0.5$ denotes the weights of RMSE and SSIM respectively, showing the relative impact of RMSE and SSIM on the combined error. $RMSE_{\text{norm}}$ is a normalized term that gives the pixel-wise difference between ground truth and synthetic images and has a value from 0 (identical) to 1 (very pixel-wisely different) for each generated design. $SSIM_{\text{norm}}$ is a normalized term that gives the overall difference between ground truth images and synthetic images and varies from 0 (identical) to 1 (very overall different). This normalization process allows for the fair assessment of the combination, ensuring that the lowest RMSE and the highest SSIM were represented by consistent values. We seek to determine the most favorable combination of RMSE and SSIM as a measure of accuracy of the models. We address this multi-objective decision-making by developing a combined error function that combines RMSE and SSIM errors. The objective is to minimize the combined error, which in practice means searching for a combination that achieves the lowest RMSE while maximizing SSIM simultaneously. Fig. 7b shows the combined error for each model, indicating that T100 has the lowest combined error. This outcome signifies that T100 exhibits the highest level of accuracy. Achieving this level of accuracy with only 100 training images highlights the significant advantages of our approach compared to the conventional deep learning methods. For instance, Zhenze et al. required a dataset of 2000 paired training composite configurations to achieve acceptable accuracy when using the cGAN method to predict the stress or strain field binary composites microstructure [61]. Gu et al. generated a total of 80,000 random microstructures as the training data to predict composite material employing CNN [62]. Mann et. al used 12,800 training configurations to capture highly non-linear microstructure-property in high contrast composite material systems by developing a new CNN architecture [63]. Kim et al. developed a CNN-based model aimed

at predicting the transverse mechanical behavior of unidirectional composites. This model uses 9000 microstructure images as input datasets to predict the stress-strain curves of the composites in the transverse direction [64]. These numbers are orders of magnitude larger than the size of data set we use. While our method focuses on predicting stress distribution in various complex IPCs, as opposed to the studies mentioned that predict mechanical properties, we are optimistic that our approach has the potential to pave the way for the development of data-efficient methods for predicting the correlation between mechanics and structure.

We also observe that T2 model, using just 2 training images, can produce stress fields and composite structures although they exhibit lower accuracy compared to the T100 model. T2 model struggles to predict stress concentration regions within the stress field but is proficient in showing the overall Von Mises stress distribution in both rigid and soft phases. This distinction underscores the significance of our model, which can achieve its performance with just two training images, highlighting its efficiency and non-dependence on extensive data.

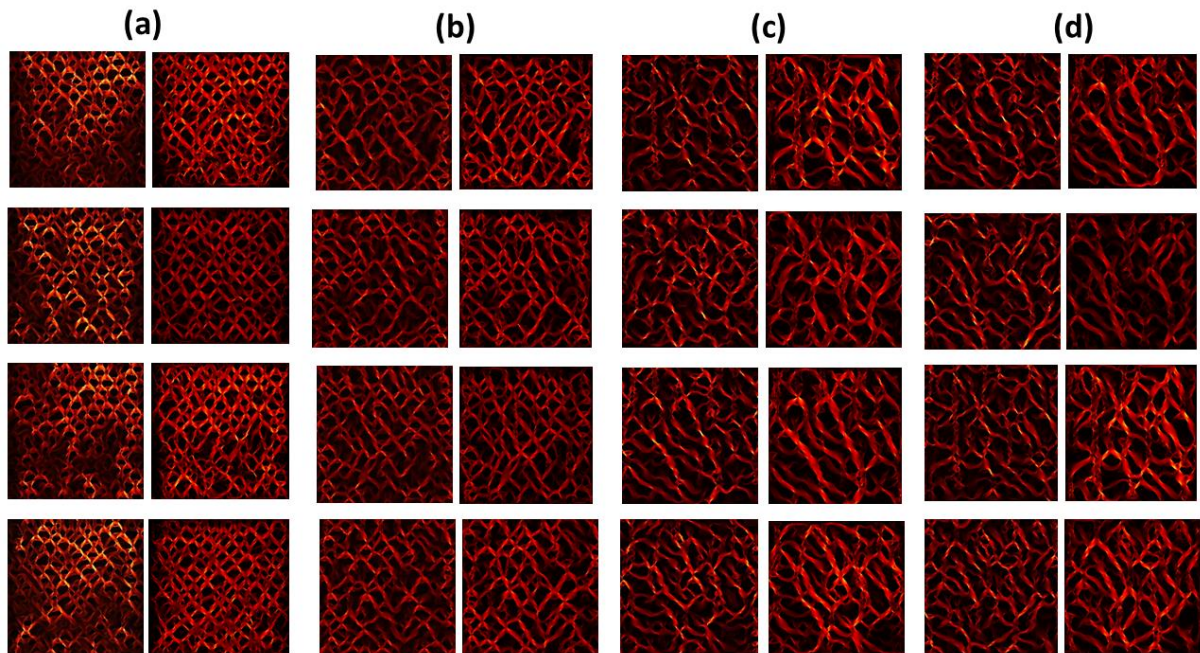


Figure 6: Comparison of synthetic and ground truth images for models trained with different numbers of images: (a) T2 (trained with 2 images), (b) T50 (trained with 50 images), (c) T100 (trained with 100 images), and (d) T150 (trained with 150 images). Each pair of images consists of a synthetic image (left) and a ground truth image (right). Visually, there is no significant difference in the accuracy of the models with increasing training dataset size. However, with more training data, the design space learned by the model expands, enabling the generation of more diverse structures. In contrast, models trained with fewer images show a tendency to become biased towards the training data, resulting in a smaller design space.

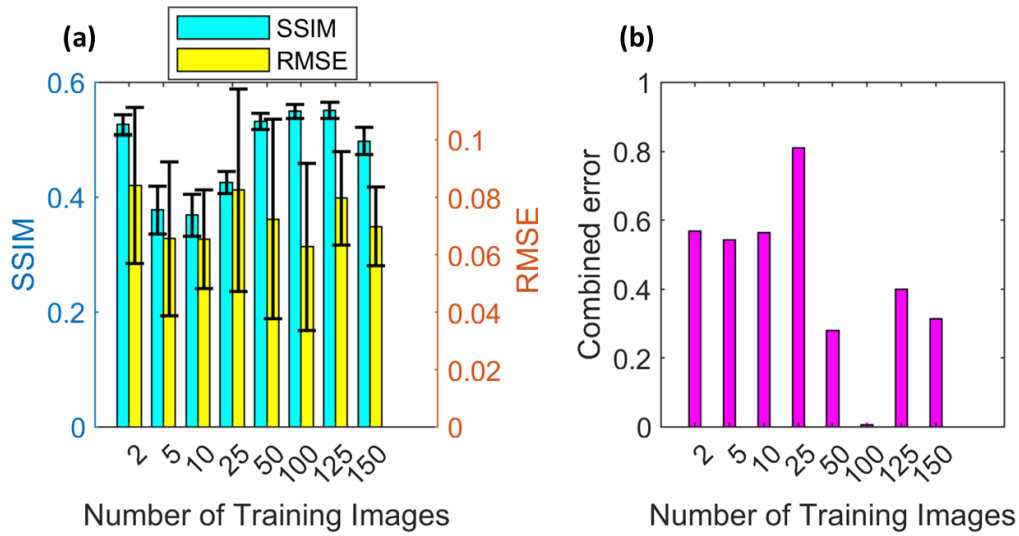


Figure 7: Comparison of (a) normalized RMSE and SSIM and (b) Combined error for the models with different number of training images, computed with Eq. (19). All other hyperparameters such as optimizer type, learning rate, network architecture remains the same for different models.

4 CONCLUSIONS

In this study, we effectively combined Molecular Dynamics and generative AI techniques, enabled through SD, to design and rapidly predict the stress fields of complex composites under mechanical load, demonstrating the powerful synergy between these components. By leveraging MD simulations for initial data generation and employing the high-dimensional data-learning capabilities of SD, particularly through LoRA, we have effectively created an AI model to rapidly find and utilize structure-mechanics correlation to design complex IPC structures. We demonstrate that outputs of multiscale modeling can finely tune generative AI models. It forms a rapidly evolving technique that can understand and massively produce distinctive designs in response to simple natural language instructions. This tool will, therefore, reduce the technical barrier and computational amount for regular users of numerical modeling. The predicted outcome can be directly applied to composite synthesis for validation or application to broad engineering fields, including aerospace, wind energy industry, high-end automotive, healthcare, sports gear, and construction restoration, by generating coherent designs not limited by human experience or existing models or trapped by local optimal results.

Acknowledgments: The authors acknowledge the National Science Foundation Grant (Award #: 2145392), the startup funding and the Brodsky’s fund at Syracuse University in support this research work.

REFERENCES

- [1] C. Barile, C. Casavola, F. De Cillis, Mechanical comparison of new composite materials for aerospace applications, *Compos. Part B Eng.* 162 (2019) 122–128.

- <https://doi.org/https://doi.org/10.1016/j.compositesb.2018.10.101>.
- [2] M. Mrázová, Advanced composite materials of the future in aerospace industry, *INCAS Bull.* 5 (2013) 139–150. <https://doi.org/10.13111/2066-8201.2013.5.3.14>.
- [3] F. Khan, N. Hossain, J.J. Mim, S.M.M. Rahman, M.J. Iqbal, M. Billah, M.A. Chowdhury, Advances of composite materials in automobile applications – A review, *J. Eng. Res.* (2024). <https://doi.org/https://doi.org/10.1016/j.jer.2024.02.017>.
- [4] M. Schwartz, J.D. Restuccia, A.K. Rosen, Composite Measures of Health Care Provider Performance: A Description of Approaches., *Milbank Q.* 93 (2015) 788–825. <https://doi.org/10.1111/1468-0009.12165>.
- [5] M.P. Jones, A. Mautner, S. Luenco, A. Bismarck, S. John, Engineered mycelium composite construction materials from fungal biorefineries: A critical review, *Mater. \& Des.* 187 (2020) 108397. <https://api.semanticscholar.org/CorpusID:213198918>.
- [6] T. Sain, J. Meaud, G. Hulbert, E.M. Arruda, A.M. Waas, Simultaneously high stiffness and damping in a class of wavy layered composites, *Compos. Struct.* 101 (2013) 104–110. <https://doi.org/10.1016/j.compstruct.2013.01.024>.
- [7] D. Quan, R. Alderliesten, C. Dransfeld, N. Murphy, A. Ivanković, R. Benedictus, Enhancing the fracture toughness of carbon fibre/epoxy composites by interleaving hybrid meltable/non-meltable thermoplastic veils, *Compos. Struct.* 252 (2020). <https://doi.org/10.1016/j.compstruct.2020.112699>.
- [8] Q.D. To, M.T. Nguyen, G. Bonnet, V. Monchiet, V.T. To, Overall elastic properties of composites from optimal strong contrast expansion, *Int. J. Solids Struct.* 120 (2017) 245–256. <https://doi.org/10.1016/j.ijsolstr.2017.05.006>.
- [9] Y. Pu, Z. Ma, L. Liu, Y. Bai, Y. Huang, Improvement on strength and toughness for CFRPs by construction of novel “soft-rigid” interface layer, *Compos. Part B Eng.* 236 (2022) 109846. <https://doi.org/10.1016/j.compositesb.2022.109846>.
- [10] A. Shimamura, Y. Hotta, H. Hyuga, M. Hotta, K. Hirao, Improving the thermal conductivity of epoxy composites using a combustion-synthesized aggregated β -Si₃N₄ filler with randomly oriented grains, *Sci. Rep.* 10 (2020) 1–9. <https://doi.org/10.1038/s41598-020-71745-w>.
- [11] G.X. Gu, C.T. Chen, M.J. Buehler, De novo composite design based on machine learning algorithm, *Extrem. Mech. Lett.* 18 (2018) 19–28. <https://doi.org/10.1016/j.eml.2017.10.001>.
- [12] O. Diegel, A. Nordin, D. Motte, Additive Manufacturing Technologies, in: 2019: pp. 19–39. https://doi.org/10.1007/978-981-13-8281-9_2.
- [13] R. Cartwright, Book Reviews: Book Reviews, *Perspect. Public Health* 130 (2010) 239–239. <https://doi.org/10.1177/1757913910379198>.
- [14] A.R. Studart, Biological and bioinspired composites with spatially tunable heterogeneous architectures, *Adv. Funct. Mater.* 23 (2013) 4423–4436. <https://doi.org/10.1002/adfm.201300340>.
- [15] J.F.V. Vincent, Biomimetic materials, *J. Mater. Res.* 23 (2008) 3140–3147. <https://doi.org/10.1557/jmr.2008.0380>.
- [16] L. Li, C. Ortiz, Pervasive nanoscale deformation twinning as a catalyst for efficient energy dissipation in a bioceramic armour, *Nat. Mater.* 13 (2014) 501–507. <https://doi.org/10.1038/nmat3920>.
- [17] J.W.C. Dunlop, P. Fratzl, Biological composites, *Annu. Rev. Mater. Res.* 40 (2010) 1–

24. <https://doi.org/10.1146/annurev-matsci-070909-104421>.
- [18] S. Weiner, H.D. Wagner, The material bone: Structure-mechanical function relations, *Annu. Rev. Mater. Sci.* 28 (1998) 271–298. <https://doi.org/10.1146/annurev.matsci.28.1.271>.
- [19] C. Chun-Teh, J.M.-M. Francisco, L. Shengjie, Q. Zhao, J.B. Markus, Nacre-inspired design of graphene oxide–polydopamine nanocomposites for enhanced mechanical properties and multi-functionalities, *Nano Futur.* 1 (2017) 11003. <http://stacks.iop.org/2399-1984/1/i=1/a=011003>.
- [20] D. Liu, J. Song, D.P. Anderson, P.R. Chang, Y. Hua, Bamboo fiber and its reinforced composites: Structure and properties, *Cellulose* 19 (2012) 1449–1480. <https://doi.org/10.1007/s10570-012-9741-1>.
- [21] K. Tai, M. Dao, S. Suresh, A. Palazoglu, C. Ortiz, Nanoscale heterogeneity promotes energy dissipation in bone, *Nat. Mater.* 6 (2007) 454–462. <https://doi.org/10.1038/nmat1911>.
- [22] X. Li, W.C. Chang, Y.J. Chao, R. Wang, M. Chang, Nanoscale structural and mechanical characterization of a natural nanocomposite material: The shell of red abalone, *Nano Lett.* 4 (2004) 613–617. <https://doi.org/10.1021/nl049962k>.
- [23] A. Tanay, L. Bitincka, R. Shamir, E.K.O. Shea, A.I. Tschumi, R. Kishony, C.A. Telmer, S.A. Adler, C.A. Telmer, V. Subramaniam, A.J. Lopez, T.J. Mitchison, N. Perrimon, S.E. Fraser, J. Ellenberg, A.I. Lamond, J.S. Brotman, S.T. Sweeney, G. Davis, R. Daneman, M. Zavortink, W. Chia, L.F. Liu, P.D. Arpa, W.P. Pfund, V.B. Mehta, D.K. Trask, D. Makonchuk, C. Gomes, J.J. Zheng, M. Hetman, M.S. Wold, J.A. Borowiec, T.C. Elston, W.J. Blake, J.J. Collins, A.J. Levine, E.D. Siggia, P.S. Swain, M. Thattai, I. Kurtser, A.D. Grossman, A. Van Oudenaarden, S.J. Arlander, L. Karnitz, C. Lin, S.Y. Sun, S. Zhao, Z.R. Liu, W.M. Old, K.A. Resing, N.G. Ahn, M. Mann, J. Bar, I. Glinert, T. Shlapok, Tough, Bio-Inspired Hybrid Materials, (2008) 1516–1521.
- [24] L. Han, L. Wang, J. Song, M.C. Boyce, C. Ortiz, Direct quantification of the mechanical anisotropy and fracture of an individual exoskeleton layer via uniaxial compression of micropillars, *Nano Lett.* 11 (2011) 3868–3874. <https://doi.org/10.1021/nl201968u>.
- [25] B.J.F. Bruet, J. Song, M.C. Boyce, C. Ortiz, Materials design principles of ancient fisharmour, *Nat. Mater.* 7 (2008) 748–756. <https://doi.org/10.1038/nmat2231>.
- [26] D.R. Clarke, Interpenetrating Phase Composites, *J. Am. Ceram. Soc.* 75 (1992) 739–758. <https://doi.org/https://doi.org/10.1111/j.1151-2916.1992.tb04138.x>.
- [27] Y. Zhang, M.T. Hsieh, L. Valdevit, Mechanical performance of 3D printed interpenetrating phase composites with spinodal topologies, *Compos. Struct.* 263 (2021). <https://doi.org/10.1016/j.compstruct.2021.113693>.
- [28] M. Zhang, Q. Yu, Z. Liu, J. Zhang, G. Tan, D. Jiao, W. Zhu, S. Li, Z. Zhang, R. Yang, R.O. Ritchie, 3D printed Mg-NiTi interpenetrating-phase composites with high strength, damping capacity, and energy absorption efficiency, *Sci. Adv.* 6 (2020) 1–9. <https://doi.org/10.1126/sciadv.aba5581>.
- [29] M. Zhang, N. Zhao, Q. Yu, Z. Liu, R. Qu, J. Zhang, S. Li, D. Ren, F. Berto, Z. Zhang, R.O. Ritchie, On the damage tolerance of 3-D printed Mg-Ti interpenetrating-phase composites with bioinspired architectures, *Nat. Commun.* 13 (2022) 1–13.

- <https://doi.org/10.1038/s41467-022-30873-9>.
- [30] M.J. Buehler, Atomistic and continuum modeling of mechanical properties of collagen: Elasticity, fracture, and self-assembly, *J. Mater. Res.* 21 (2006) 1947–1961. <https://doi.org/10.1557/jmr.2006.0236>.
- [31] M. Masrouri, Z. Qin, Effects of terminal tripeptide units on mechanical properties of collagen triple helices, *Extrem. Mech. Lett.* 64 (2023) 102075. <https://doi.org/10.1016/j.eml.2023.102075>.
- [32] M. Jiang, C.-H. Yu, Z. Xu, Z. Qin, Binding of Carbon Monoxide to Hemoglobin in an Oxygen Environment: Force Field Development for Molecular Dynamics, *J. Chem. Theory Comput.* (2024). <https://doi.org/10.1021/acs.jctc.4c00029>.
- [33] J. Schmidt, M.R.G. Marques, S. Botti, M.A.L. Marques, Recent advances and applications of machine learning in solid-state materials science, *Npj Comput. Mater.* 5 (2019) 83. <https://doi.org/10.1038/s41524-019-0221-0>.
- [34] L. Wang, J. Boddapati, K. Liu, P. Zhu, C. Daraio, W. Chen, Mechanical cloak via data-driven aperiodic metamaterial design, *Proc. Natl. Acad. Sci.* 119 (2022) e2122185119. <https://doi.org/10.1073/pnas.2122185119>.
- [35] G.X. Gu, C.-T. Chen, M.J. Buehler, De novo composite design based on machine learning algorithm, *Extrem. Mech. Lett.* 18 (2018) 19–28. <https://doi.org/https://doi.org/10.1016/j.eml.2017.10.001>.
- [36] A. Ramesh, P. Dhariwal, A. Nichol, C. Chu, M. Chen, Hierarchical Text-Conditional Image Generation with CLIP Latents, (2022).
- [37] C. Saharia, W. Chan, S. Saxena, L. Li, J. Whang, E. Denton, S.K.S. Ghasemipour, B.K. Ayan, S.S. Mahdavi, R. Gontijo-Lopes, T. Salimans, J. Ho, D.J. Fleet, M. Norouzi, Photorealistic Text-to-Image Diffusion Models with Deep Language Understanding, *Adv. Neural Inf. Process. Syst.* 35 (2022).
- [38] J.-R. Anna, Artificial intelligence as part of future practices in the architect’s work: MidJourney generative tool as part of a process of creating an architectural form, *Architectus* 3 (2022) 95–104. <https://doi.org/10.37190/arc220310>.
- [39] R. Rombach, A. Blattmann, D. Lorenz, P. Esser, B. Ommer, High-Resolution Image Synthesis with Latent Diffusion Models, *Proc. IEEE Comput. Soc. Conf. Comput. Vis. Pattern Recognit.* 2022-June (2022) 10674–10685. <https://doi.org/10.1109/CVPR52688.2022.01042>.
- [40] G. Zhou, S. Xie, G. Hao, S. Chen, B. Huang, X. Xu, C. Wang, L. Zhu, L. Yao, K. Zhang, Emerging Synergies in Causality and Deep Generative Models: A Survey, 14 (2023) 1–22.
- [41] N. Dehouche, K. Dehouche, What’s in a text-to-image prompt? The potential of stable diffusion in visual arts education., *Heliyon* 9 (2023) e16757. <https://doi.org/10.1016/j.heliyon.2023.e16757>.
- [42] A. Blattmann, R. Rombach, H. Ling, T. Dockhorn, S.W. Kim, S. Fidler, K. Kreis, Align Your Latents: High-Resolution Video Synthesis with Latent Diffusion Models, *Proc. IEEE Comput. Soc. Conf. Comput. Vis. Pattern Recognit.* 2023-June (2023) 22563–22575. <https://doi.org/10.1109/CVPR52729.2023.02161>.
- [43] J. Ackermann, M. Li, High-Resolution Image Editing via Multi-Stage Blended Diffusion, (2022).
- [44] J. Ho, A. Jain, P. Abbeel, Denoising diffusion probabilistic models, *Adv. Neural Inf.*

- Process. Syst. 2020-Decem (2020) 1–12.
- [45] S. Zhang, Z. Qian, K. Huang, R. Zhang, J. Xiao, Y. He, C. Lu, Robust generative adversarial network, *Mach. Learn.* 112 (2023) 5135–5161. <https://doi.org/10.1007/s10994-023-06367-0>.
- [46] L. Yang, Z. Zhang, Y. Song, S. Hong, R. Xu, Y. Zhao, W. Zhang, B. Cui, M.-H. Yang, Diffusion Models: A Comprehensive Survey of Methods and Applications, 1 (2022). <http://arxiv.org/abs/2209.00796>.
- [47] Z. Shi, AI Application to Generate an Expected Picture Using Keywords with Stable Diffusion, *J. Artif. Intell. Pract.* 6 (2023) 66–71. <https://doi.org/10.23977/jaip.2023.060110>.
- [48] H. Fausk, D.C. Isaksen, Improving Language Understanding by Generative Pre-Training, *Homol. Homotopy Appl.* 9 (2007) 399–438.
- [49] E. Hu, Y. Shen, P. Wallis, Z. Allen-Zhu, Y. Li, S. Wang, L. Wang, W. Chen, Lora: Low-Rank Adaptation of Large Language Models, *ICLR 2022 - 10th Int. Conf. Learn. Represent.* (2022) 1–26.
- [50] J. Howard, S. Ruder, Universal Language Model Fine-tuning for Text Classification, (2018).
- [51] B. Lester, R. Al-Rfou, N. Constant, The Power of Scale for Parameter-Efficient Prompt Tuning, *EMNLP 2021 - 2021 Conf. Empir. Methods Nat. Lang. Process. Proc.* (2021) 3045–3059. <https://doi.org/10.18653/v1/2021.emnlp-main.243>.
- [52] J. Devlin, M.-W. Chang, K. Lee, K. Toutanova, BERT: Pre-training of Deep Bidirectional Transformers for Language Understanding, in: *North Am. Chapter Assoc. Comput. Linguist.*, 2019.
- [53] M.J. Buehler, MechGPT, a Language-Based Strategy for Mechanics and Materials Modeling That Connects Knowledge Across Scales, Disciplines, and Modalities, *Appl. Mech. Rev.* 76 (2024). <https://doi.org/10.1115/1.4063843>.
- [54] R.K. Luu, M.J. Buehler, BioinspiredLLM: Conversational Large Language Model for the Mechanics of Biological and Bio-Inspired Materials, *Adv. Sci.* 11 (2024) 2306724. <https://doi.org/https://doi.org/10.1002/advs.202306724>.
- [55] E.L. Buehler, M.J. Buehler, X-LoRA: Mixture of Low-Rank Adapter Experts, a Flexible Framework for Large Language Models with Applications in Protein Mechanics and Design, (2024).
- [56] C. Zhao, Y. Ogawa, S. Chen, Z. Yang, Y. Sekimoto, Label Freedom: Stable Diffusion for Remote Sensing Image Semantic Segmentation Data Generation, *Proc. - 2023 IEEE Int. Conf. Big Data, BigData 2023* (2023) 1022–1030. <https://doi.org/10.1109/BigData59044.2023.10386381>.
- [57] M. Masrouri, Z. Qin, Towards data-efficient mechanical design of bicontinuous composites using generative AI, *Theor. Appl. Mech. Lett.* 14 (2024) 100492. <https://doi.org/https://doi.org/10.1016/j.taml.2024.100492>.
- [58] S. Plimpton, Fast Parallel Algorithms for Short-Range Molecular Dynamics, *Soft Matter* 14 (1994) 2–19. <https://doi.org/10.1039/c7sm02429k>.
- [59] A. Stukowski, Visualization and analysis of atomistic simulation data with OVITO-the Open Visualization Tool, *Model. Simul. Mater. Sci. Eng.* 18 (2010). <https://doi.org/10.1088/0965-0393/18/1/015012>.
- [60] AUTOMATIC1111, “Stable Diffusion Web UI,” (2022).

- [61] Z. Yang, C.-H. Yu, M.J. Buehler, Deep learning model to predict complex stress and strain fields in hierarchical composites, *Sci. Adv.* 7 (2021) eabd7416. <https://doi.org/10.1126/sciadv.abd7416>.
- [62] G.X. Gu, C.-T. Chen, D.J. Richmond, M.J. Buehler, Bioinspired hierarchical composite design using machine learning: simulation{,} additive manufacturing{,} and experiment, *Mater. Horiz.* 5 (2018) 939–945. <https://doi.org/10.1039/C8MH00653A>.
- [63] A. Mann, S.R. Kalidindi, Development of a Robust CNN Model for Capturing Microstructure-Property Linkages and Building Property Closures Supporting Material Design, *Front. Mater.* 9 (2022). <https://doi.org/10.3389/fmats.2022.851085>.
- [64] D.-W. Kim, J.H. Lim, S. Lee, Prediction and validation of the transverse mechanical behavior of unidirectional composites considering interfacial debonding through convolutional neural networks, *Compos. Part B Eng.* 225 (2021) 109314. <https://doi.org/https://doi.org/10.1016/j.compositesb.2021.109314>.